aerospace

MDPI

Article

Computational Tool for Aircraft Fuel System Analysis

Marcela A. D. Di Marzo [1,2,*], Pedro G. Calil [1], Hossein Nadali Najafabadi [2], Viviam Lawrence Takase [3], Carlos H. B. Mourão [3] and Jorge H. Bidinotto [1]

[1] Department of Aeronautics Engineering, University of São Paulo (USP), São Carlos 13566-590, Brazil; pedro.gcalil11@gmail.com (P.G.C.); jhbidi@sc.usp.br (J.H.B.)
[2] Applied Thermodynamics and Fluid Mechanics (MVS) Division, Linköping University (LiU), 581 83 Linköping, Sweden; hossein.nadali.najafabadi@liu.se
[3] EMBRAER S.A.—Engineering and Technology, Gavião Peixoto 14813-000, Brazil; viviam.lawrence@embraer.com.br (V.L.T.); chbmourao@gmail.com (C.H.B.M.)
* Correspondence: marcelademarzo@usp.br

Abstract: Fuel level gauging in aircraft presents a significant flight mechanics challenge due to the influence of aircraft movements on measurements. Moreover, it constitutes a multidimensional problem where various sensors distributed within the tank must converge to yield a precise and single measurement, independent of the aircraft's attitude. Furthermore, fuel distribution across multiple tanks of irregular geometries complicates the readings even further. These issues critically impact safety and economy, as gauging errors may compromise flight security and lead to carrying excess weight. In response to these challenges, this research introduces a multi-stage project in aircraft fuel gauging systems, as a continuum of studies, where this first article presents a computational tool designed to simulate aircraft fuel sensor data readings as a function of fuel level, fuel tank geometry, sensor location, and aircraft attitude. Developed in an open-source environment, the tool aims to support the statistical inference required for accurate modeling in which synthetic data generation becomes a crucial component. A discretization procedure accurately maps fuel tank geometries and their mass properties. The tool, then, intersects these geometries with fuel-level planes and calculates each new volume. It integrates descriptive geometry to intersect these fuel planes with representative capacitive level-sensing probes and computes the sensor readings for the simulated flight conditions. The method is validated against geometries with analytical solutions. This process yields detailed fuel measurement responses for each sensor inside the tank, and for different analyzed fuel levels, providing insights into the sensors' signals' non-linear behavior at each analyzed aircraft attitude. The non-linear behavior is also influenced by the sensor saturation readings at 0 when above the fuel level and at 1 when submerged. The synthetic fuel sensor readings lay the baseline for a better understanding on how to compute the true fuel level from multiple sensor readings, and ultimately optimizing the amount of used sensors and their placement. The tool's design offers significant improvements in aircraft fuel gauging accuracy, directly impacting aerostructures and instrumentation, and it is a key aspect of flight safety, fuel management, and navigation in aerospace technology.

Keywords: aircraft fuel systems; aircraft fuel gauging; fuel quantity estimation; sensor data simulation; fuel probe readings signals; synthetic data generation; fuel system modeling; flight attitude impact analysis

Citation: Di Marzo, M.A.D.; Calil, P.G.; Najafabadi, H.N.; Takase, V.L.; Mourão, C.H.B.; Bidinotto, J.H. Computational Tool for Aircraft Fuel System Analysis. *Aerospace* **2024**, *11*, 362. https://doi.org/10.3390/aerospace11050362

Academic Editor: Konstantinos Kontis

Received: 18 February 2024
Revised: 17 April 2024
Accepted: 23 April 2024
Published: 1 May 2024

1. Introduction

Over the decades, aircraft performance has gone through great improvements in several areas. The fuel systems have developed from a simple set of tanks, feeding the engine through gravity, and gauged by float-driven indicators to a complex set of tank geometries, with multi-valve systems, booster pumps, and several sensors [1].

Beyond dealing with more efficient and complex engine feeding, refueling, and defueling operations, the fuel system should also be prepared to transfer fuel among its tanks, and to safely dump fuel outside the aircraft in emergency situations [2]. Additionally, fuel also plays an important role in aircraft thermal management systems, serving as the main material for absorbing and dispersing heat from the aircraft [3]. For that, it must be capable of incorporating its complexity, by having a well-designed Fuel Quantity Gauging System (FQGS), in order to be accurate in indicating the real fuel tank quantity to the flight crew.

Furthermore, FQGSs are exposed to many situations that make the challenge of being accurate even harder. Events such as aircraft attitude changes, acceleration, turbulence, and structural deformation due to aerodynamic loads during flight affect the final fuel quantity indication [1].

The accuracy of the FQGS is compromised by these factors, in which the aircraft attitude changes present a significant challenge that this computational tool aims to address.

Even small errors in fuel quantity measurement can imply a significant impact on the costs of the aircraft throughout its operation life. As an example, we can take an aircraft with a fuel capacity of approximately 100 tons, the Boeing 777–200. It carries between 305 and 328 passengers in a typical three-class configuration and has a total fuel capacity of 201,700 pounds (93,900 kg). Under these conditions, 1% of error is equivalent to almost 1 ton, which represents approximately 10 passengers with their luggage [4]. Therefore, it is of great interest to the aircraft's manufacturer and operators to accomplish precision of the FQGS.

Recognizing the significant impact that even minor inaccuracies in fuel measurement can have underscores the pressing need for more advanced and precise solutions in fuel management systems. In modern days, the rapid evolution of technology, particularly in computational capabilities and Artificial Intelligence (AI), offers a promising avenue for addressing these challenges. As we continue to witness unparalleled growth in accessible computational resources [5], the opportunity arises to harness this technological momentum to develop more sophisticated and accurate methods for fuel quantity estimation in aviation.

Due to this, modeling and simulating complex systems enables higher accuracy in systems' description/prediction, taking into account several variables, and being able to represent real-life behavior [6].

As AI and computational capabilities continue to advance, they offer novel solutions to longstanding challenges in aviation [7]. Numerous areas within the industry stand to benefit substantially from AI integration. Recent studies have explored how these technologies can revolutionize the sector, ranging from enhancing customer experiences to enabling more intelligent and cost-effective design and operational strategies [8–13].

In the realm of fuel systems, AI technology offers significant potential for enhancement, particularly in addressing the challenge of accurate fuel quantity measurement. This task, essential for providing pilots with reliable data across varying aircraft attitudes and fuel property fluctuations, represents a complex, multidimensional estimation problem [14]. It involves transforming a collection of sensor signals into a singular one, a precise fuel quantity estimation. Traditionally, this transformation in embedded systems is achieved through one-dimensional, linearly interpolated look-up tables [14]. However, this study aims to, through large generative synthetic readings data, allow innovation beyond this conventional approach by integrating and applying machine learning models for more dynamic and accurate estimations.

In this context, to aid AI modeling and enhance the learning process for accurate fuel quantity estimation, there is a critical need for diverse sensor data, reflecting various aircraft conditions and fuel levels. To circumvent the challenges of acquiring such extensive real-world sensor readings, this article proposes the development of a computational tool designed for generating synthetic fuel sensor data. This approach not only addresses the immediate data needs but also facilitates collaborative innovation. By utilizing synthetic data, partners such as aircraft manufacturers, airlines, sensor developers, and academic

institutions can collectively advance data processing technologies while safeguarding sensitive intellectual property.

The development of this computational tool for generating synthetic sensor data is crucial due to several key reasons:

- **Promoting Collaborative Innovation with Partners:** Synthetic data facilitates collaborative innovation in data processing technologies by allowing partners to work together without risking the exposure of sensitive intellectual property.
- **Developing Robust Models for Diverse Scenarios:** The synthetic data generated by this tool is crucial in creating advanced models capable of accurately capturing a multitude of operational scenarios as the attitude of the aircraft changes. This capability is essential for developing a more refined and precise model for fuel estimation, ensuring that fuel quantity readings remain reliable under a wide range of flight conditions. Such models are crucial for both operational efficiency and safety.
- **Advancing Fuel Gauging System Efficiency:** The tool is instrumental in researching and developing more efficient fuel gauging systems. It facilitates precise placement and optimization of probes within the system, ensuring more accurate and reliable fuel measurements.
- **Optimizing Probe Combinations:** By enabling experimentation with various probe combinations, the tool helps identify the most effective configurations for fuel measurement. This optimization leads to improved accuracy and efficiency in fuel gauging systems.
- **Enhancing Academic Research:** The tool is a valuable asset for academic research, providing the capability to generate a wide array of synthetic sensor data for generic fuel systems. Researchers can use any tank geometry, even those not based on actual aircraft, to study the relationship between fuel levels and sensor behavior in different scenarios. This flexibility enriches the understanding of fuel measurement dynamics and supports educational objectives.
- **Open-Source Development for Wider Accessibility:** The entire development of this tool in an open-source format ensures its accessibility to a broad range of users. This approach not only democratizes access to advanced research tools but also encourages community-driven improvements and innovations.
- **Environmental Impact and Safety Enhancement:** By enabling more accurate fuel quantity estimations, the tool contributes to reducing unnecessary fuel carriage, thereby decreasing environmental impact. Additionally, precise fuel measurement is crucial for flight safety, enhancing the overall safety standards in aviation.

Many authors have studied the challenges in the fuel system area. Zhu et al. [15] highlight the importance of the fuel system and the challenges in its measurement; they also proposed other techniques to try to overcome this problem, such as image analysis and processing. Two authors, Lee et al. [16] and Oliveira et al. [17], employ statistical techniques to measure fuel uncertainty, with Lee et al. applying a Markov Chain Monte Carlo method for fuel quantity estimation in supplementary aircraft tanks [16]. This approach utilized data from a test simulator, underlining the importance of synthetic data generation tools.

Uzun el al. [18] tried to combine physics-guided deep-learning models with fuel consumption modeling in an attempt to improve data-driven models' consistency exactly in conditions where it is not covered by data, showing, first the importance of having data, and second, that combining domain knowledge with advanced computational techniques can significantly enhance the accuracy and reliability of fuel measurement systems in aviation, further supporting the objectives of this project.

Oliveira et al. [17] also used a Monte Carlo method, but for calculating measurement uncertainty in solid-oxide fuel cells. Additionally, Cui et al. [19] emphasize the advantage of adopting AI tools, such as Artificial Neural Networks, for quantifying fuel savings, showing the competitiveness of a data-driven model; this reasoning, moreover, can be adopted in the fuel quantity estimation process, thus minimizing the fuel carried in excess. While efforts like those by Uzun et al. [18] explore merging physics-guided principles with

machine learning in fuel consumption modeling, this project emphasizes the crucial role of comprehensive data availability. Additionally, Na and Zhi-Hong [20] address the problem of fuel measurement by focusing on the other difficulty in fuel measuring, the estimation of remaining fuel volume in aircraft, suggesting improvements to neural network algorithms to enhance accuracy.

In this context, this project has the main objective of creating a framework that allows the engineer to import a given 3D aircraft tank (or a set of them), and the sensors' coordinates, and combine the tank geometry discretization with linear algebra in order to obtain the relationship between the tank fuel level in each attitude and the corresponding sensors' signal. The development target is a script on Python 3.8 to generate the synthetic dataset to be later adopted in the learning process.

This tool can generate a set of data that can be used to train models and support engineering in the decision-making process on the design of an aircraft FQGS [21].

The developed computational tool is validated using basic geometries such as the cubic and the spherical shapes that inhere well-understood analytical behavior, allowing straightforward comparisons that ensure the tool's results are reliable. Section 4 presents the volumetric estimation results for these two types of fuel tanks, firstly the cubic tank and secondly the spherical one.

Subsequently, simplified capacitive sensors were integrated into the cubic tank system. This allowed for a comparison between the tool's readings and the expected values. The system was then rotated 90 degrees to assess the tool's accuracy under altered conditions. Finally, a more realistic aircraft fuel tank, as depicted in Figure 1, was employed to further test the tool's capabilities and to generate the required data.

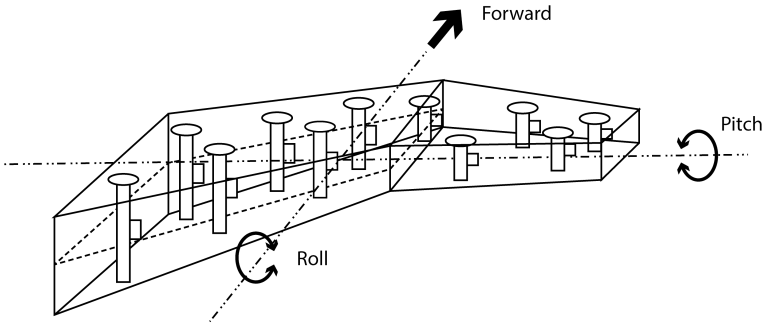

Figure 1. Example of a simplified aircraft wing tank. Adapted from [1].

2. Theoretical Background

With the evolution of aircraft, new and more complex fuel systems were required. Since this system is the largest fluid system of an aircraft, it is commonly composed of several tanks that define the amount of fuel that an aircraft can store. This quantity determines how far an aircraft can fly, and its precise measurement is required for a safe flight [1,22,23].

2.1. Aircraft Fuel Tanks

As the fuel system is a crucial component of any aircraft, its design plays a critical role in the certification and in the operational aspects of the aircraft [2]. As its main function, this system must feed the engines with a reliable supply of fuel at appropriate pressures and flows but, in some cases, it also takes an important role ensuring that the center of gravity of the aircraft remains within the lateral and longitudinal envelope limits, by moving fuel among tanks [23,24].

In general, a fuel system is comprised of tanks, booster and transfer pumps, valves, strainers, and pressure and level sensors [1,25]. For this study, as its goal is to analyze the

fuel level gauging, only the set of fuel tanks and the level sensors were considered in the modeling of the system.

Aircraft tank geometries can have many different shapes, normally being irregular, which contributes to making the task of measuring fuel difficult. Its shape depends mainly on the aircraft's purpose and model, being hard to determine, especially in the initial stages of the aircraft design [1].

In order to demonstrate the many geometries that a tank can have, it is possible to mention three main types of tank: the rigid removable tanks, the bladder tanks, and the integral fuel tanks [24,26].

An example of an irregular integral fuel tank geometry, represented by a simplified aircraft wing fuel tank, can be seen in Figure 1.

In addition to the common geometry irregularity, the fuel level quantification is aggravated by the fact that the tank will follow the aircraft rotation when the aircraft's attitude changes. The fuel level measurement is also impacted by the accelerations to which the aircraft is submitted. However, when it is under constant accelerations, it is possible to calculate an equivalent "pitch and roll" so that a model without accelerations can be used. This challenge is taken under this research study case.

2.2. Fuel Level Sensors

The primary purpose of a fuel level measurement system in aircraft is to accurately assess the fuel quantity in the tanks, a crucial factor that significantly influences fuel management system decisions and, consequently, impacts both the safety and economic efficiency of flight operations. The developed tool focuses on **capacitive sensors**, the most commonly used type in turbine-powered aircraft, ensuring precise data analysis for these systems [1,24–29]. While specifically tailored for capacitive sensors, adapting this tool for other types of sensors would require modifications to the underlying algorithms and data processing techniques.

This type of sensor is composed of two mutually insulated concentric cylindrical plates and has a method based on the difference between the dielectric constant of the liquid (fuel) and of the air above it, in which the height of the fuel is measured in relation to the total height of the plate [30–32].

The basic operating principle of capacitive sensors for level detection by capacitance works when the dielectric medium (in this case fuel) is introduced between the two electrodes. In this way, as the liquid level changes the dielectric between the electrodes also changes, so it is possible to detect the two different capacitances: the first capacitor being formed by the liquid as dielectric, and the second one being formed by the air as dieletric [33]. An example of this sensor is shown in Figure 2.

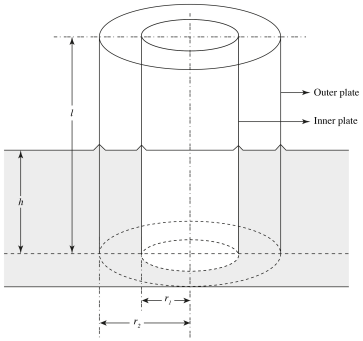

Figure 2. Typical capacitive sensor [30].

As shown in Figure 2, l is the total length of the plates and h is the portion of the sensor that is submerged in fuel. According to the operational conditions of this type of

sensor, the space between the electrodes, $s = r_2 - r_1$, must be much less than the radius of the inner electrode, r_1, in which s is the distance between the toroidal dielectric, that is, the space between the concentric cylindrical plates. Furthermore, the tank height, l, should be much greater than r_2.

For the purpose of our capacitive sensor model, the term r_c is to be understood as the radius of the inner electrode, which is identical to r_1 as specified in the operational conditions; hence, r_c and r_1 are used interchangeably. In this conditions, the capacitance (C) can be expressed by Equation (1):

$$C = \frac{\varepsilon_l(l) + \varepsilon_g(h-l)}{4.6log[l-(s/r_c)]}, \tag{1}$$

in which ε_l and ε_g are the dielectric constants of the liquid (fuel) and the gas (air), respectively [30]. As the variable of interest is h, Equation (1) can be rearranged to (2):

$$C = \frac{\varepsilon_l - \varepsilon_g}{4.6log[l-(s/r_c)]}l + \frac{\varepsilon_g}{4.6log[l-(s/r_c)]}h. \tag{2}$$

Apart from h, all parameters in Equation (2) are constants or properties that depend on the probe's dimensions and the fuel and air dielectric constants. These terms are related to the fixed system. Therefore, the sensor's capacitance can be simplified to:

$$C = C_{dry} + K_{fuel}h, \tag{3}$$

in which C_{dry} is the sensor's capacitance when completely dry and K_{fuel} is a constant that depends on the fuel's dielectric constant and the fixed probe's dimensions.

As the capacitance varies with the wet length h, the variation can be expressed by Equation (4):

$$\delta C = K_{fuel}\delta h. \tag{4}$$

It is possible to conclude from Equation (4) that the relation of measured capacitance and the depth immersion h is directly proportional. Given this information, the quantity of fuel inside the tank can be estimated as a function of the depth immersion h for one or more probes.

2.3. Euler Angles Rotation

The aircraft attitude changes can be simulated as a rotation of a non-inertial reference frame that follows the aircraft's body around an inertial one, fixed on Earth. In the aeronautics community, the pitch attitude angle is usually represented by θ, the roll attitude angle by ϕ, and the yaw attitude angle by ψ. These three, so-called Euler Angles, are defined by the rotation angle around the Y, X, and Z axes, respectively [34,35]. This representation is shown in Figure 3.

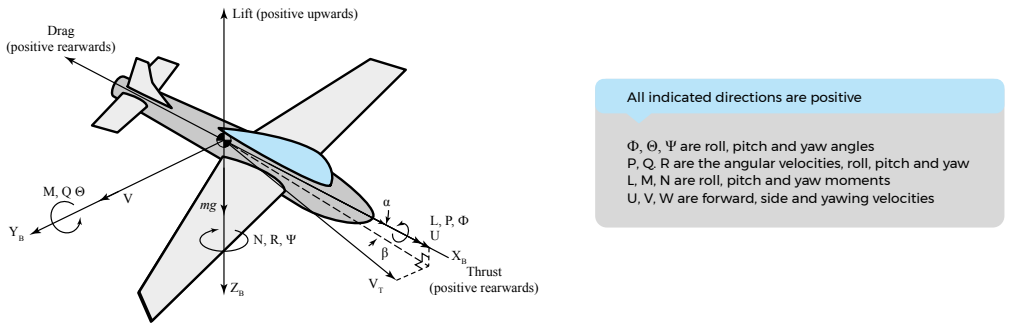

Figure 3. Typical aeronautical Euler Angles. Adapted from [34,36].

Considering a vector $\vec{v}$, represented on the inertial reference system as the components v_x^i, v_y^i, v_z^i , and the components v_x^r, v_y^r, v_z^r as the non inertial reference system. Using $S_x = sin(x)$ and $C_x = cos(x)$, the relation between the body represented in the rotated reference system and in the inertial one is [37–39]:

$$\begin{Bmatrix} v_x^i \\ v_y^i \\ v_z^i \end{Bmatrix} = \begin{Bmatrix} C_\theta C_\psi & C_\theta S_\psi & -S_\theta \\ S_\phi S_\theta C_\psi - C_\phi S_\psi & C_\phi C_\psi + S_\phi S_\theta C_\psi & S_\phi C_\theta \\ S_\phi S_\psi + C_\phi S_\theta C_\psi & C_\phi S_\theta S_\psi - S_\phi C_\psi & C_\phi C_\theta \end{Bmatrix} \begin{Bmatrix} v_x^r \\ v_y^r \\ v_z^r \end{Bmatrix}. \quad (5)$$

In the tool herein described, every component of the aircraft—the fuel tank by itself, the fuel surface, and the capacitive probes—are described by vectors. Therefore, any aircraft's attitude change is represented as a rotation of every element of the system with the same Euler Angles within the support of Equation (5).

2.4. Geometry Discretization Procedure

The discretization process is a fundamental step in computational geometry, essential for converting complex geometric forms into a numerically manageable format [40]. It is widely used together with several solving methods for simulating and understanding the behavior of structures, solids, and fluids [41].

In this study, the focus of discretization is on the fuel tank geometries, transforming them into a series of discrete elements (meshing) . This approach enables detailed modeling and analysis of the tanks, crucial for accurate simulations of their physical properties.

In practical terms, the tanks were represented as meshes composed of triangular elements of constant mass density. The triangulation process represents a point set through triangles that intersect only at shared vertices and edges [42]. Figure 4 shows the visualization of the triangulation made, for example, on a sphere surface.

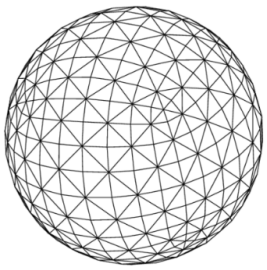

Figure 4. Surface triangulation of a sphere [43].

To calculate the relevant tank's mass properties for the simulation, such as the volume and center of gravity, the tool uses the Trimesh https://trimsh.org/trimesh.html (accessed on 1 March 2021) and Numpy-STL https://pypi.org/project/numpy-stl/ (accessed on 1 March 2021) Python libraries. The solving methods used in these libraries are described in [44,45] and in their documentation.

To slice the triangular mesh with a plane, it was employed a straightforward approach: calculating the intersections of each triangle edge with the plane and generating new vertices at these intersection points. Subsequently, vertices above the plane were discarded, and the mesh surface was recalculated to reflect these changes.

It is important to note that the tool does not use any structural analysis, such as finite element methods, so there is no need for the analyses of specific element types, topology, or boundary conditions. It is also important to highlight that the tool does not even discretize the mesh, rather it is an input of it.

2.5. Fuel Level Sensors Signals

For a specific attitude (pitch and roll), considering the surface of the fuel inside the tank as a flat plane, the capacitance reading of each sensor in the tank will be determined by the length from the submerged end until the intersection with the fuel plane (h), as can

be seen in Figure 5. Each capacitive fuel probe is modeled in this project as a finite line, defined by its two extreme coordinates.

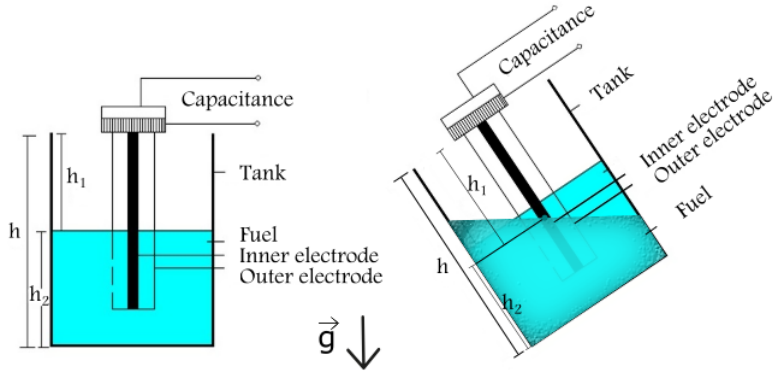

Figure 5. Visualization of the interaction between the capacitive sensor and the fuel plane (perpendicular and inclined). Adapted from [33].

Inclinations under 30 degrees do not add significant errors when adopting this simplification [46].

To better describe the next steps of the study, a brief explanation about relative position between lines and planes will be presented. There are three possible cases of relative position between lines and planes: the plane intersects the line, the plane contains a line, or the plane is parallel to the line. In the first case, the plane must have only one common point with the line, whereas in the second one it must have at least two common points, and in the third one it does not have any common points [47–49]. The three cases can be seen in Figure 6a, 6b, and 6c, respectively.

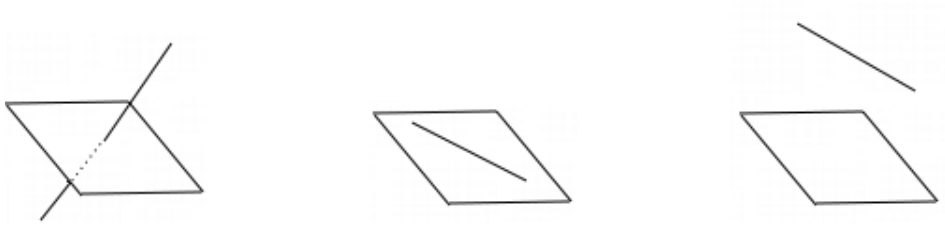

(**a**) (**b**) (**c**)

Figure 6. Cases of relative position between lines and plane. (**a**) Intersection between line and plane. (**b**) Plane contains a line. (**c**) Plane parallel to a line.

Given a vector $\vec{v} = (m, n, p)$ parallel to a line $r \subset E^3$ that contains a point $A = (x_0, y_0, z_0) \in r$, r can be described by $r : (x, y, z) = (x_0, y_0, z_0) + \lambda(m, n, p), \lambda \in \mathbb{R}$. To calculate the relative position between r and a plane with general equation $ax + by + cz + d = 0$, the following system needs to be solved through Cramer Rule [50]:

$$\begin{cases} 1.x + 0y + 0z - m\lambda = x_0 \\ 0x + 1.y + 0z - n\lambda = y_0 \\ 0x + 0y + 1.z - p\lambda = z_0 \\ ax + by + cz + 0\lambda = -d \end{cases} \tag{6}$$

This system has only one solution if

$$\begin{vmatrix} 1 & 0 & 0 & -m \\ 0 & 1 & 0 & -n \\ 0 & 0 & 1 & -p \\ a & b & c & 0 \end{vmatrix} \neq 0 \tag{7}$$

and calculating this determinant, $am + bn + cp \neq 0$. Hence, if this is true, the system can be solved and the plane intersects the line in the point (x, y, z) that resolves the system (6). Otherwise, the plane can be either parallel or contains the line. Then, it is necessary to verify if the plane contains any point of the line, so if $ax_0 + by_0 + cz_0 + d = 0$, then the plane contains r, else they are parallel [48,49].

3. Simulation Methods

To simulate how the volume of fuel changes and how this is interpreted by the capacitive probes, a set of geometric files, with "Standard Triangle Language" (*.stl) extension, were imported in Python through the two already mentioned open source libraries, Trimesh https://trimsh.org/trimesh.html (accessed on 1 March 2021) and Numpy-STL https://pypi.org/project/numpy-stl/ (accessed on 1 March 2021).

The use of these two similar libraries was essential due to their complementary functionalities; neither one alone could fulfill all the requirements needed for the project's comprehensive development. Additionally, it is noteworthy that both libraries lack the capability to import a single file containing multiple geometric shapes. As a result, each tank in the system must be represented in a separate file, and these files are then imported individually into the tool.

Required Inputs

For simulating capacitive probes (refer to Section 2.2), the user must provide a $(n, 2, 3)$ array for each tank, where n denotes the number of probes in the respective tank. Each array consists of coordinate pairs representing the start and end points of each probe; the initial point given by (x_0, y_0, z_0) and the final point by (x_1, y_1, z_1). Thus, the structure of the probe's array is as follows:

$$\begin{Bmatrix} (x_0^1, y_0^1, z_0^1) & (x_1^1, y_1^1, z_1^1) \\ (x_0^2, y_0^2, z_0^2) & (x_1^2, y_1^2, z_1^2) \\ \cdot & \\ \cdot & \\ \cdot & \\ (x_0^n, y_0^n, z_0^n) & (x_1^n, y_1^n, z_1^n) \end{Bmatrix}. \tag{8}$$

Another necessary input for the tool is the set of attitude angles, ϕ, ψ, and θ (Section 2.3), that is going to be simulated. Let V_ϕ, V_ψ, and V_θ be the vectors that contain all roll, yaw, and pitch angles, respectively, considered in the simulation. The length of the set calculated by the Cartesian product [51] $V_\phi \times V_\psi \times V_\theta$ will be defined by i-th roll, j-th yaw, and w-th pitch positions, as described by Equation (9):

$$V_\phi \times V_\psi \times V_\theta = \{(\phi_i, \psi_j, \theta_w) : \phi_i \in V_\phi, \psi_j \in V_\psi, \theta_w \in V_\theta\}, \tag{9}$$

in which this cartesian product defines the number of simulation interactions that the tool will perform in the system. In order for the tool to successfully perform the system rotation, it is important to provide (by the user) the coordinates of the point where the tool should rotate the system around. Otherwise, it will rotate around the tank's center of gravity (calculated by the libraries) [35,37].

The simulation consists of describing the behavior of the probes according to different fuel level conditions. For that, it is considered a static model, since it is possible to calculate an equivalent "pitch and roll" in the case of constant accelerations. So, in this case, an equivalent attitude is incorporated into the model for study. Therefore, it is considered that the surface of the fluid is a plane whose normal vector is parallel to the gravitational force vector [52]. Considering the axis as in Figure 3, the gravity acceleration is $(0, 0, 1) \times g$, hence vector $(0, 0, 1)$ is normal to every fuel surface. As a plane can be described by $ax + by + cz + d = 0$ in which (a, b, c) is the normal vector of the plane [53], the general equation of the planes that describes all fuel surfaces will be:

$$0x + 0y + 1z + d = 0, \tag{10}$$

$$z + d = 0. \tag{11}$$

To define the general equation of each surface level that contains a point (x_P, y_P, z_P), it is necessary to replace its coordinates in Equation (11),

$$z_P + d = 0, \tag{12}$$

$$d = -z_P, \tag{13}$$

replacing (13) in (11),

$$z - z_P = 0. \tag{14}$$

The last information required to start the simulation is the number of surface levels, n_{levels}, that will be considered in each tank. For each surface condition, the real amount of fuel and the percentage of wet height in each probe is calculated.

With the tank system imported as a mesh and all initial parameters defined, the first step is to loop through the set defined by Equation (9) and for each angle's set to perform the process described below.

To simulate the attitude motion of the aircraft, it is necessary to apply Equation (5) for the probe's array (Equation (8)), the four arrays that define Trimesh and the three arrays that define Numpy-STL meshes. From this point on, only the rotated arrays will be considered for the tool.

As the simulation occurs independently for each tank in the system, the next steps can be parallelized to maximize the usage of the computational resources.

Let Z_{tank} be a vector that contains the coordinates of the axis Z of all vertices of the triangles in the tank *mesh*. Considering the axis as described in Figure 3, the top-most point, z_{top}, and the bottom-most point, z_{bottom}, are calculated by

$$z_{top} = min\{Z_{tank}\}, \tag{15}$$

$$z_{bottom} = max\{Z_{tank}\}. \tag{16}$$

As the simulation considers the tank from its completely empty state up to its completely full state, the first surface level contains z_{bottom} and the last contains z_{top}. Taking h_{step} as the distance between each surface level, and considering that this value remains constant for a set of angles and a tank, the set of all surface levels, from Equation (14), is defined by:

$$\{z - (z_{bottom} - x.h_{step}) = 0 : x \in \mathbb{N}, 0 \leq x \leq n_{levels} - 1\}, \tag{17}$$

in which h_{step} is

$$h_{step} = \frac{z_{bottom} - z_{top}}{n_{levels} - 1}. \tag{18}$$

The initial analyses and visualizations were performed using both a sphere and a cube, with each shape effectively illustrating different steps of the same process. The cube and sphere were chosen to clearly demonstrate the fuel surfaces and the slicing procedure, making it easier for readers to grasp the concepts. We begin by showcasing the cube, oriented at $(\phi, \psi, \theta) = (0, 0, 0)$ and with $n_{levels} = 5$, as depicted in Figure 7.

To calculate the real amount of fuel for each one of the surfaces, the mesh is sliced by the respective plane and its volume is calculated (Section 2.4). The result of this slicing process is shown in Figure 7 (on the cube) and Figure 8 (on the sphere).

To calculate the wet height percentage of each probe in each surface level, it is necessary to find the relative position between the line that contains the probe and the plane that contains the fuel surface (Section 2.5). For that, the general equation of the plane (Equation (17)), a vector parallel to the probe's line, and a point in this line are necessary.

Given the initial point of the probe, $P = (x_0, y_0, z_0)$, and the final one, $Q = (x_1, y_1, z_1)$, in which $z_1 =< z_0$, the vector $\vec{v} = (x_1 - x_0, y_1 - y_0, z_1 - z_0)$ is parallel to a line that contains P and Q [53].

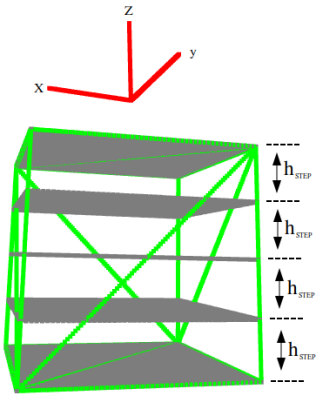

Figure 7. Fuel surfaces in a cube.

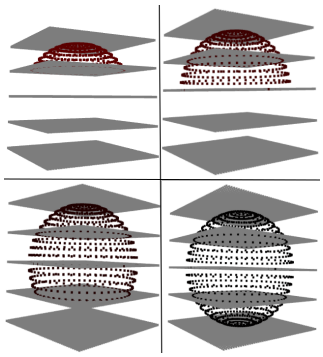

Figure 8. Slicing stages of a sphere.

With the relative position calculated, it is possible to determine how the capacitive probe measures the fuel level. It has two main cases: (1) if the line intersects the plane, being non-parallel to the plane; or (2) if the line is parallel to the plane.

1. The non-parallel line classification: it can be broken down into three subcases:
    1.1. intersection above the upper point of the probe;
    1.2. intersection below the lower point of the probe;
    1.3. intersection between the upper and lower points.
2. The parallel line classification: it can be unfolded into two subcases:
    2.1. when the plane contains the line;
    2.2. when the plane does not contain the line, which by itself can be divided into two further cases:
        i the line is below the fuel surface;
        ii the line is above the fuel surface.

These seven different situations are described below:

1. If the plane intersects the plane (the non-parallel case):
    1.1. If the plane intersects the line below the bottom-most point of the probe: in this case, if the plane in height z_{Plane} intersects the line in a point $I = (x_I, y_I, z_I)$, in which $z_{Plane} = z_I$ and $z_{Plane} \leq z_1 < z_0$, it means that the surface level is below the bottom-most part of the probe, hence it will measure 0.

1.2. If the plane intersects the line above the top-most point of the probe ($z_{Plane} \geq z_0 > z_1$), then the surface level is above the top-most part of the probe, hence it will be fully submerged in fuel, measuring 1.

1.3. If the plane intersects the line between the top-most point and the bottom-most point of the probe ($z_1 < z_{Plane} < z_0$), then the surface level slices the probe, so its percentage of depth immersion will be the ratio between the distance from the intersection point and the bottom-most part of the probe and its entire length [48,49], as described by Equation (19):

$$\frac{|\vec{PI}|}{|\vec{v}|} = \frac{\sqrt{(x_I - x_0)^2 + (y_I - y_0)^2 + (z_I - z_0)^2}}{\sqrt{(x_1 - x_0)^2 + (y_1 - y_0)^2 + (z_1 - z_0)^2}}. \quad (19)$$

2. If the line is parallel to the fuel plane:

2.1. If the plane in height z_{Plane} is parallel to the line and contains it, then the fuel surface is exactly in the same level as the probe and contains it entirely. In this case, it was adopted that the probe's measurement is equal to 1, as it was completely submerged in fuel;

2.2. If the plane in height z_{Plane} is parallel to the line, but does not contain it, then $z_1 = z_0$. In this case, there are two different possibilities:

i If $z_{Plane} < z_1$, it means that the probe is completely submerged in fuel. Therefore, its measurement is 1;

ii Otherwise, it will be completely dry, measuring 0.

A summary of the developed tool is depicted in Figure 9.

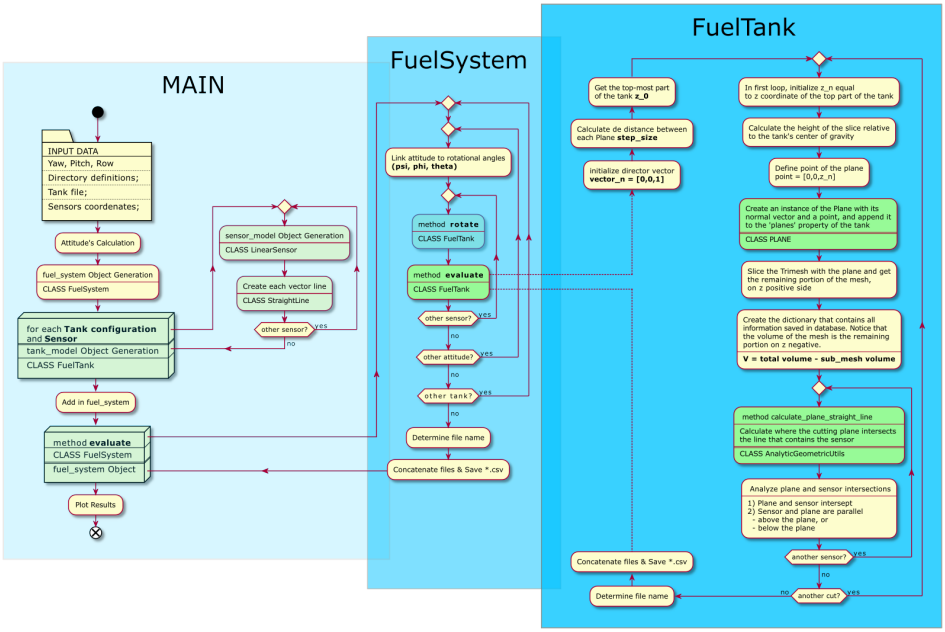

Figure 9. Visual flowchart of the developed algorithm, which details the programming sequence and decision points. The initial square at the top-left corner outlines the input data required. Progression through the algorithm's steps is indicated by arrows. Green boxes highlight critical operations, such as the instantiation of objects upon class invocation and the execution of methods for performing calculations. Diamond-shaped symbols (parallelograms) signify conditional checks, representing decision points that could result in a loopback for additional processing, determining the need for further sensors, tanks, or attitudes to be calculated. Symmetrical lozenges (rhombuses) indicate the points where the loop restarts after these checks. The use of color coding and geometric shapes emphasizes the structural elements and the dynamic flow of the algorithmic process.

4. Results and Discussion

The first step to validate the tool was to check if the slicing process is able to properly calculate the real amount of fuel in each surface level, and the second one was to apply the tool in a more realistic tank topology. The volume calculated by the tool was compared to the analytical volume of a sphere with radius $R = 50$, and a cube with edge length $L = 20$. Both geometries had $n_{slices} = 100$. For the sphere, in each surface level the tank is a spherical cap with height $h = |z_{Plane} - z_{bottom}|$ and radius R. The volume of a spherical cap (V_{cap}) is described by Equation (20) [54].

$$V_{cap} = \frac{1}{3}\pi h^2(3R - h). \tag{20}$$

The comparison results are shown in Figure 10.

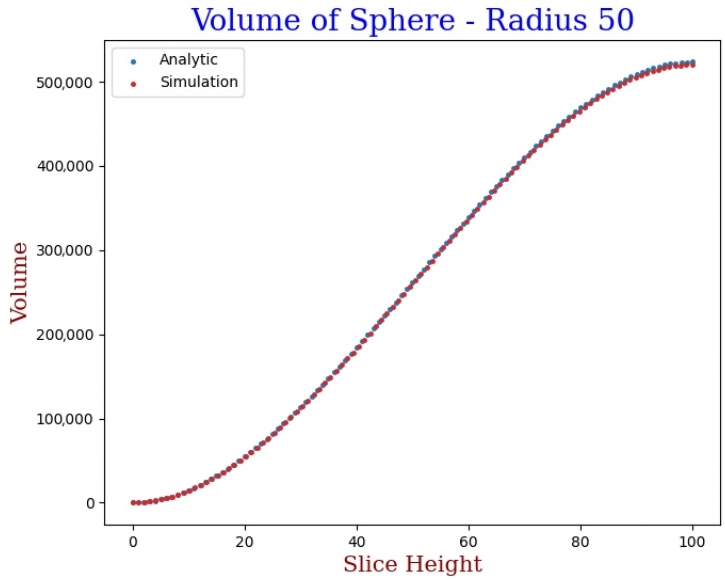

Figure 10. Comparison between analytic and simulation results on a sphere with radius 50.

Considering the volume calculated in the simulation as $V_{simulation}$ and the analytical volume as $V_{analytical}$, the considered Percentage Error (PE) of the simulation is

$$PE = \frac{|V_{simulation} - V_{analytical}|}{V_{analytical}} \times 100. \tag{21}$$

The error behavior can be seen in Figure 11.

Notice that near the "Slice Height" zero, that is, for slices very close to the bottom of the mesh, the code estimates a volume with higher errors, above 4%. This happens because, on one hand a sphere is a complex geometry (curved solid), which is difficult to represent by a triangular mesh, and on another, as these slices are too near to the bottom of the structure (where the analyzed volume is really low) a minor difference between the volume calculated by the tool and the analytical one can cause large percentage errors. Furthermore, after the 19th slice the error decreases to less than 1% and then floats around 0.5% until the end of the mesh.

It is important to highlight that the quality of the geometric structure approximation, described through the mesh, is conditioned by the number of elements contained in the *.stl file. This means that a finer mesh resolution might cause a reduction in this error. Therefore, it is possible to say that there are several approximation errors involved in the process, such as the mesh resolution (from the *.stl input) and the process of slicing the geometry and reconstructing it for the corresponding fuel level.

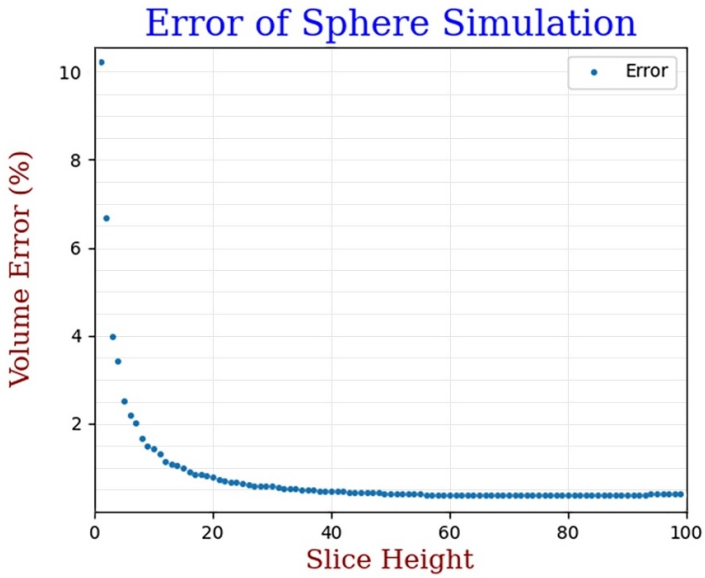

Figure 11. Error of simulation results on a sphere with radius 50.

For the cube, each surface level generates a right prism with a square face $A_{face} = L^2$ and height $h = |z_P - z_{bottom}|$. Its volume is given by Equation (22) [54].

$$V_{prism} = A_{face} \times h. \tag{22}$$

The comparison results are shown in Figure 12, and the error for the simulation with the cube, using Equation (21), is shown in Figure 13.

For the cube, during the entire simulation the error remains below 1×10^{-8} (in the order of computational numerical error scale). As the geometry of a cube is much simpler than the one of a sphere, the mesh can better represent this structure and the slicing process is much more efficient in simulating the new form of the prism. Therefore, its mass properties are calculated much more efficiently.

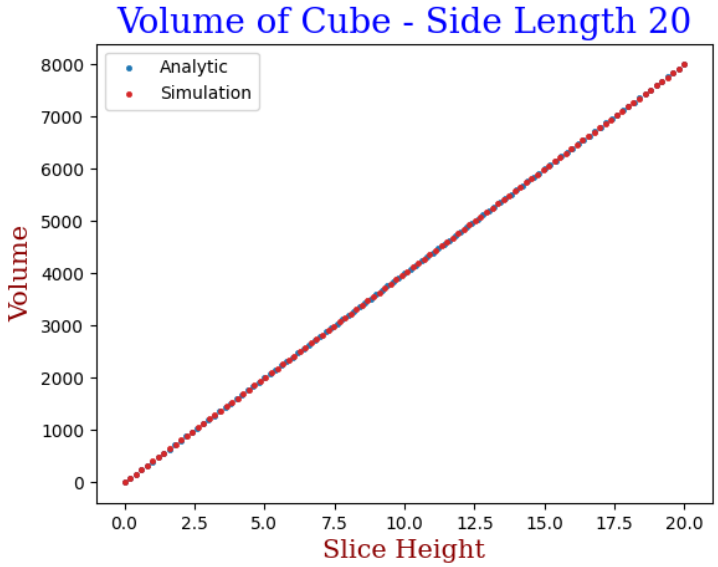

Figure 12. Comparison between analytic and simulated results on a cube with edge length 20.

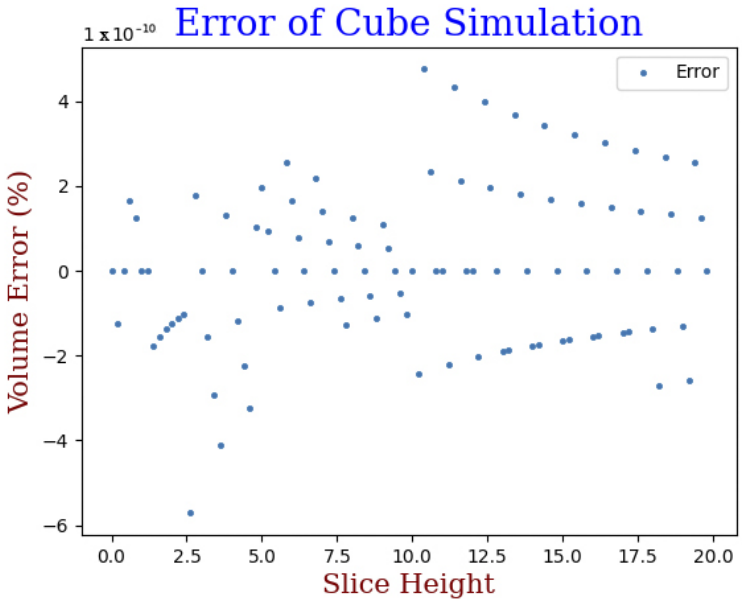

Figure 13. Simulated results error on a cube with edge length 20.

4.1. Mesh Sensitivity Analysis and Computational Performance

In this study, the CAD models for the geometries were created in SolidWorks (version 2021), licensed by Linköping University (LiU), Sweden, and exported in the STL format. However, it is important to note that the geometry can be developed using any CAD software as long as the final output is in the STL format, which is the format input to the computational tool developed in this research.

The surface triangulation generated by the CAD solver can vary in density. The accuracy and computational cost of the method have been evaluated with respect to the density of surface triangulation and its impact on volume calculation and on the slicing process.

According to Table 1 and Figure 14, the error decreases with an increase in the number of Surface Triangulations (ST); however, even for the standard mesh, for the overall volume calculation, the analytical solution yields $V_{analytical}$ = 523,598.78 mm^3, while the tool's volume calculation results in $V_{simulation}$ = 523,494.94 mm^3, leading to a discrepancy of 1358.036 mm^3. This represents a percentage difference of 0.2593%, which, given the inherent limitations of numerical simulations and the precision of computational tools, can be considered negligible and indicative of high accuracy in practical engineering and scientific applications.

Table 1. Computational performance and mesh sensitivity.

Mesh (Sliced 100 Times)	Element Amount	Computational Time Performance (s)	Error-Total Volume (%)
MESH 0	6162	0.930527	0.2593650
MESH 1	12,210	1.119006	0.1320104
MESH 2	24,492	2.045513	0.06621147
MESH 3	82,368	6.784857	0.01983154

Note: Computational performance and mesh sensitivity values for a sphere geometry with R = 50 mm.

Note that for volumes close to zero, less than 1×10^{-2} mm^3, the estimated error can be neglected because it does not have an impact on the process. Furthermore, when the actual volume is very small, any small numerical error in the volume calculation can result in a high percentage error. This is not necessarily indicative of poor computational performance; rather, it is a mathematical consequence of how the percentage error is being calculated. Alternative ways like absolute error, adjusted relative error with a threshold, or omitting small volumes from the analysis can provide better error representation.

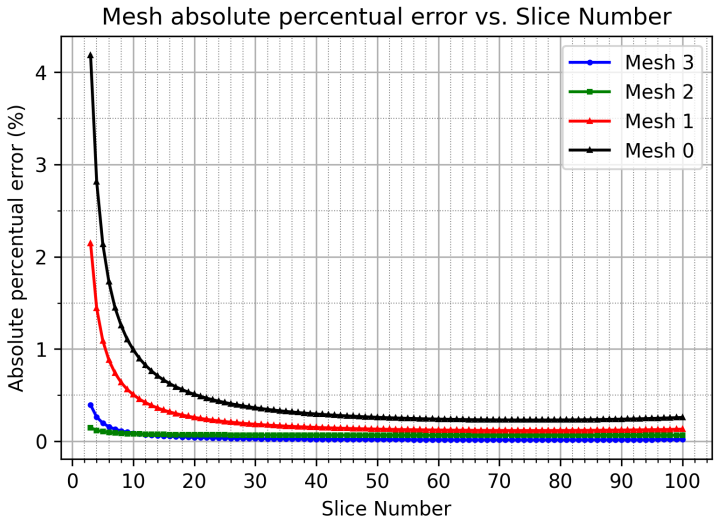

Figure 14. Mesh absolute percentage error versus slice number.

The table also highlights the method's low computational cost; for the highest mesh density, the total calculation time was approximately 6.8 s. For the generic wing tank (one of the simulated geometries results in Section 4.2.3), including slicing the geometry 500 times and simulating readings for 8 sensors, for 77 attitudes, the final execution time was approximately 2 min and 5 s, even on standard hardware. This underscores the substantial computational efficiency and robustness of the computational tool.

The outputs from this model lay the groundwork for a machine-learning algorithm that will be designed to predict volume in the next stage of our research. In this sense, real-time operation is not a requirement at this point, and there is no necessity for particularly rapid calculations. The shift to real-time functionality will occur once we implement the fully trained model within aircraft systems. This step will mark the transition to embedding our developed technology in a live operational environment.

4.2. Simulations in Other Topologies

The capacitive probes' behaviors were simulated in three different tank topologies: the first one is a right quadrangular prism, as shown in Figure 15; the second one is a multiple tank system, detailed in Section 4.2.2 *"Multiple Tank System"*; and the third one is a generic geometry of a wing tank, based on a small aircraft with a positive dihedral. This last shape is detailed in Section 4.2.3 *"Generic Wing Tank"*.

4.2.1. Right Quadrangular Prism

The first topology tested was a right quadrangular prism (Figure 15). For this tank, the parameters used were:

$$b = 40; \quad l = 20; \quad h = 50,$$

and four probes were positioned inside the tank:

$$\begin{array}{lll} P_1 = (0,0,0) & P_2 = (0,20,0) & P_3 = (40,0,0) \\ P_4 = (40,20,0) & P_5 = (0,0,50) & P_6 = (0,20,50) \\ P_7 = (40,0,50) & P_8 = (40,20,50) & \end{array}$$

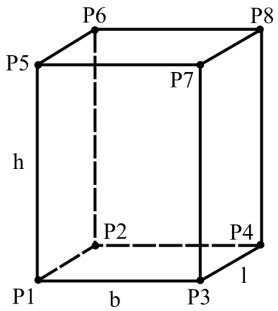

Figure 15. Right quadrangular prism. The vertices of the prism are labeled from P1 to P8. The dimensions are denoted by h for height ($h = 50$), b for base length ($b = 40$), and l for depth length ($l = 20$). The specific coordination for each vertice is described in the text.

The probes array, containing the x,y, and z coordinates of each sensor's upper and lower ends ($P_{coordinates}$) is described by Equation (23):

$$P_{coordinates} = \begin{Bmatrix} (20,10,0) & (20,10,50) \\ (0,0,0) & (40,20,16.667) \\ (40,0,16.667) & (0,20,33.333) \\ (40,20,33.333) & (0,0,50) \end{Bmatrix}. \quad (23)$$

The system containing the tank and the positioned probes is shown in Figure 16, with the tank geometry presented in green and the probes' positions presented in the following: probe 1 (blue), probe 2 (green), probe 3 (pink), probe 4 (orange).

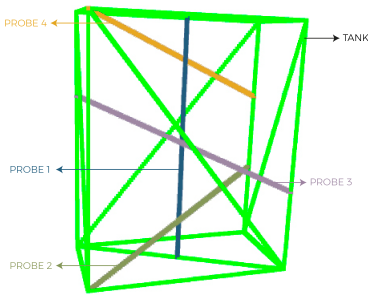

Figure 16. Quadrangular prismatic tank with probes.

By evaluating this system with $(\phi, \psi, \theta) = (0,0,0)$ and $n_{levels} = 100$, the probe's result is shown in Figure 17.

In regards to Figure 17a, referring to the first probe ($P_1 = \{(20,10,0)\ (20,10,50)\}$), as it is in a central point, perpendicular to the quadrangular base, and covers the whole height of the tank, its measure behaves as expected: measuring 0 when the tank is completely empty, increasing linearly until the top, and reaching 1 at its maximum height, when it is completely full.

The second sensor, Figure 17b, with coordinates $P_2 = \{(0,0,0)\ (40,20,16.667)\}$, starts at the origin of the system and crosses diagonally up to one-third of the tank. In this case, this sensor should mark 0 in the first point, increase linearly until the slice height of 16.667, and keep measuring 1 after this point. This figure shows that this behavior is also observed.

The third sensor, in Figure 17c, related to ($P_3 = \{(40,0,16.667)\ (0,20,33.333)\}$) has lower coordinates starting at one-third of the tank and ends diagonally opposite it at two thirds. The expected result was for this probe to just start measuring the fuel when this one reached the slice height of 16.667, i.e., this probe should keep marking 0 until the fluid reaches $1/3$ of the tank. After this point, the sensor should increase linearly until $2/3$ and reaches full measuring at this stage, keeping the value of 1 until the end of the slice height. Once again, it can be seen in Figure 17c that the proposed tool is able to detect this behavior, and it marks correctly the amount of fuel inside the tank.

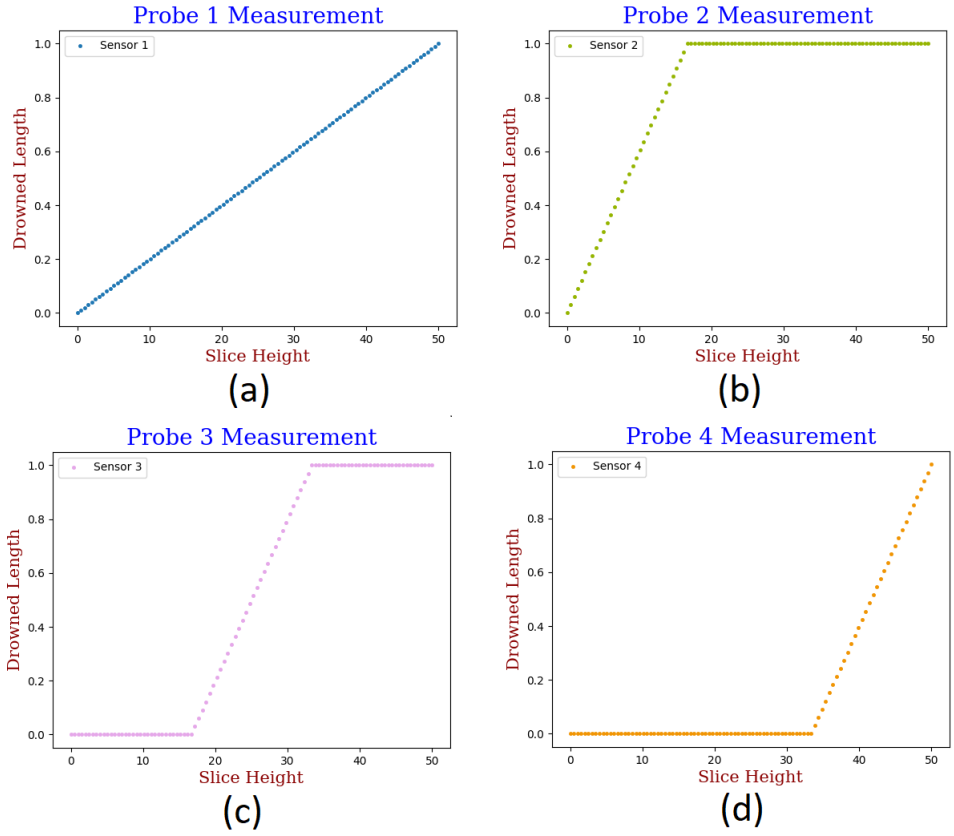

Figure 17. Measurement of system probes. Each subfigure illustrates the capacitive sensor readings that correlate drowned length with slice height. (**a**) Sensor 1's data shows a relationship between slice height and drowned length, with readings varying across the full slice height from 0 to 1 and saturation occurring only at the extremities. (**b**) Sensor 2 measurement indicates detection from 0 to $1/3$ of the tank height, beyond which it saturates at a reading of 1, suggesting a full tank. (**c**) Sensor 3's data is characterized by its measurement range between $1/3$ and $2/3$ of the tank height, with readings saturated at 0 below this interval and at 1 beyond it. (**d**) Sensor 4's data reveals measurements starting after $2/3$ of the tank height, with a saturated reading of 0 prior to this point and an increasing trend towards 1 as the tank reaches full capacity. Different colors are used to visually distinguish the readings from each sensor.

For the final probe, with coordinates $P_4 = \{(40, 20, 33.333)\ (0, 0, 50)\}$, the sensor just starts measuring the fluid when it reaches $2/3$ of the tank, previously marking zero (completely empty), in which it starts to increase linearly until the end of the tank, marking completely full (1) in the last slice height. This behavior can be checked in Figure 17d.

By rotating this system around the tank's center of gravity, $CG = (20, 10, 25)$, with $(\phi, \psi, \theta) = (90°, 0, 90°)$, the following condition is achieved (Figure 18).

Notice that, in black, there is the original tank, whereas in green and blue there is the rotated one and its probes, respectively. By evaluating this new system, the result is shown in Figure 19.

In this rotated system, the first sensor (P_1) is parallel to the fuel plane. In this case, the sensor must mark zero (0) until the slice just below its height, and mark one (1) when it reaches its coordinate, continuing to mark this measurement until the end of the tank height. In other words, in this case the sensor will switch abruptly from 0 (totally empty) to 1 (completely full).

The other sensors (P_2, P_3, P_4) in this rotated situation will have the same behavior, once all of them are located in the same way: they now have the starting point at the bottom of the tank and the end point at the top of it, with the same inclinations. These four behaviors can be seen in Figure 19.

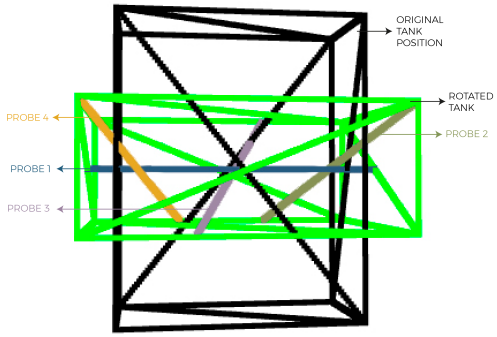

Figure 18. Rotated system vs. original.

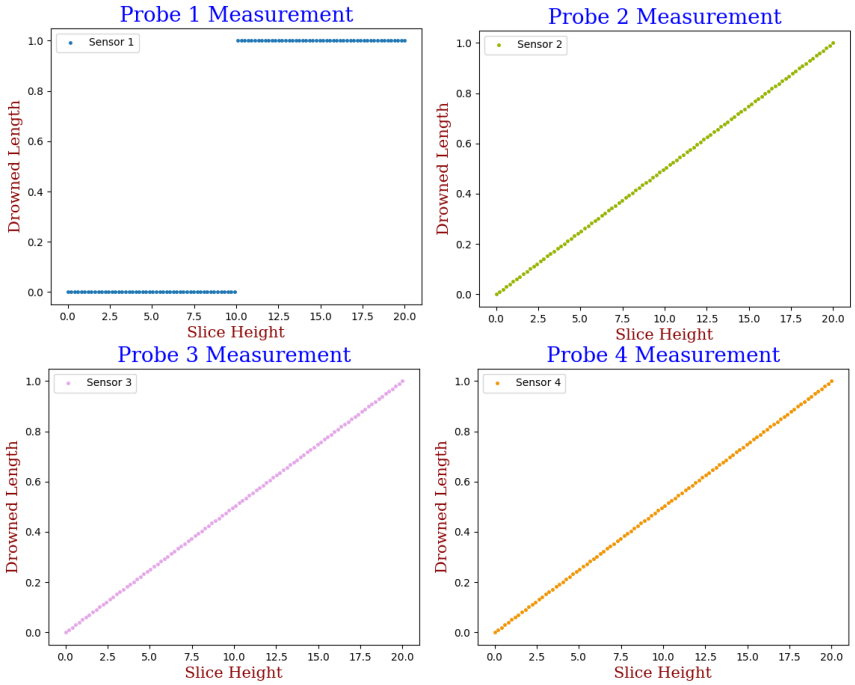

Figure 19. Measurement of rotated system probes.

4.2.2. Multiple Tank System

The tool prediction in the multiple tank system was investigated using a set of cubic tanks, T_1, T_2, T_3, T_4, with side length $L = 20$ and center coordinates $(25, 0, 0)$, $(-25, 0, 0)$, $(0, 42, 0)$, and $(0, -42, 0)$, respectively. Each tank contains a single probe, with the following arrays:

$$T_1 : \{(35, -10, 10) \quad (15, 10, -10)\}; \tag{24}$$

$$T_2 : \{(-15, 10, 10) \quad (-35, -10, -10)\}; \tag{25}$$

$$T_3 : \{(0, 42, 10) \quad (0, 42, -10)\}; \tag{26}$$

$$T_4 : \{(0, -32, 0) \quad (0, -52, 0)\}. \tag{27}$$

The system is shown in Figure 20. Considering the center of gravity in $(0, 0, 0)$, an evaluation was made with $(\phi, \psi, \theta) = (-20°, 0, -20°)$ and $n_{levels} = 100$. The rotated system can be seen in Figure 21.

The probe measurements are shown in Figure 22, which shows that, even for different aircraft attitude angles, and for aircraft with multiple fuel tanks, the tool proposed in this study is still able to show reliable quantity indications, predicting the fluid behavior inside the fuel tanks.

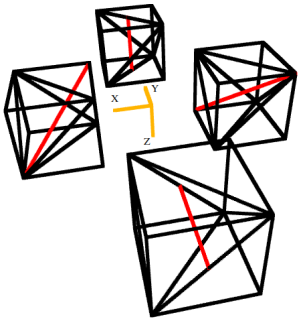

Figure 20. Multiple tank system. Each black cube represents a tank within the system, and the red line within each cube denotes the capacitive sensor.

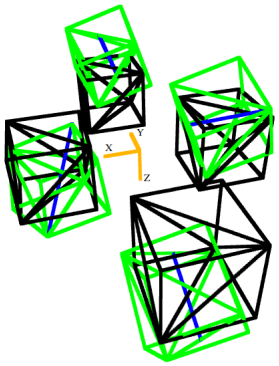

Figure 21. Rotated multiple tank system. The black cube represents the original, non-rotated tank system. The green cubes signify the same system under rotation, demonstrating the new orientation of the tanks. The blue lines within the green cubes illustrate the sensors, which have been rotated along with their respective tanks.

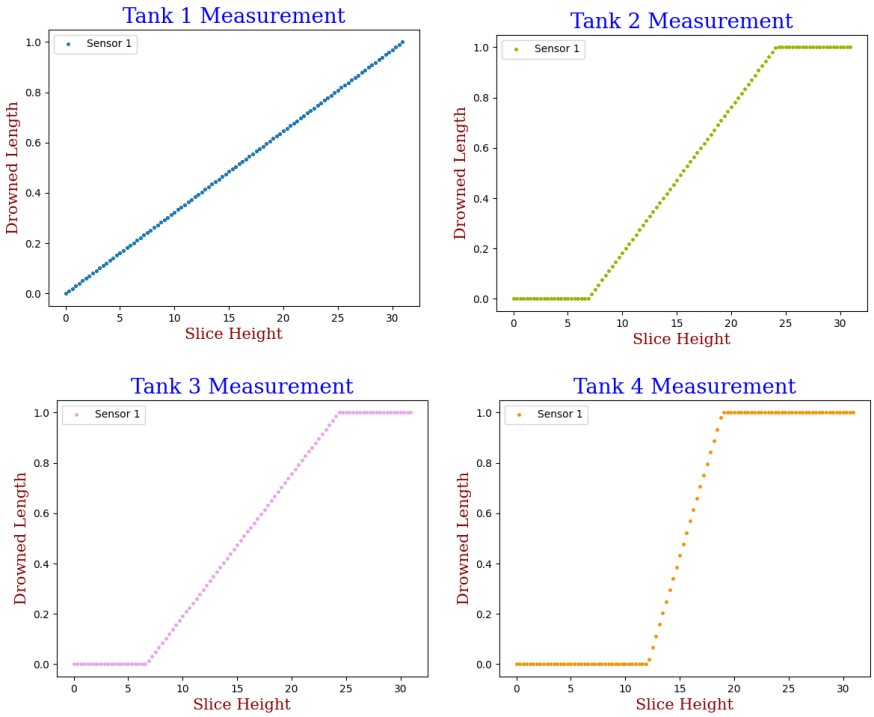

Figure 22. Probe behavior in multiple tank system.

4.2.3. Generic Wing Tank

After showing the tool's robustness and in order to achieve the final goal of this whole development (to generate synthetic data from each sensor inside an aircraft fuel tank), a simulation in a more realistic topology was required. Therefore an internal-wing fuel tank shape was designed, one that is commonly used to store fuel in aircraft, and a positive dihedral was adopted. This design was based on a small aircraft and designed using a CAD software. Figure 23 shows this fictitious tank, designed for this specific study case.

It is important to mention that eight sensors were placed randomly across this topology to simulate the capability of the system to gauge the fuel level through the wet length of each sensor, varying from 0 to 1. The developed framework enables the generation of a dataset for further studies, such as sensor position optimization, gaugeable system optimization, etc.

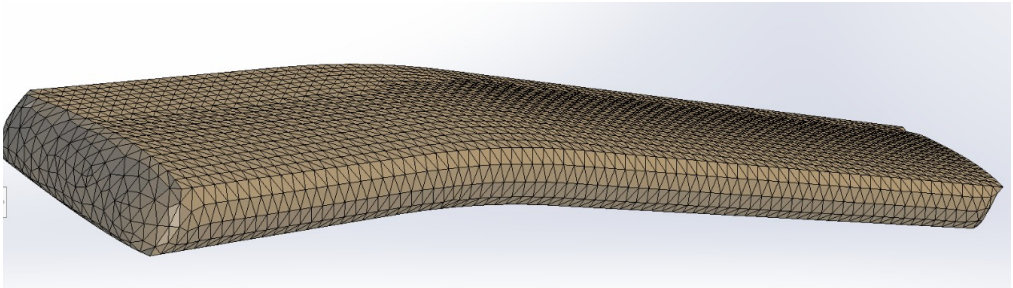

Figure 23. Tank geometry discretized with a triangular element mesh, applied in the tank topology adopted in this study.

For illustration purposes, the slicing and rotation processes of this tank geometry are depicted in Figure 24. For instance, it was considered five surface planes, and four different attitudes, the combination of the angles: Pitch = $[-15, 15]$ and Roll = $[-6, 6]$. This Figure shows the tank (in green), the surface plane cuts (in gray), and the simulated probes (in blue lines), as follows:

- Figure 24a Tank sliced in the attitude (P = 15, R = 6);
- Figure 24b Tank sliced in the attitude (P = -15, R = 6);
- Figure 24c Tank sliced in the attitude (P = 15, R = -6);
- Figure 24d Tank sliced in the attitude (P = -15, R = -6).

Additionally, we considered 77 different attitudes to explore the response of the sensors and their non-linear interactions. Each attitude was a combination of the following angles:

$$\text{Pitches: } \{-15, -12, -9, -6, -3, 0, 3, 6, 9, 12, 15\} \text{ degrees,}$$
$$\text{Rolls: } \{-6, -4, -2, 0, 2, 4, 6\} \text{ degrees,}$$

and we also adopted 500 equidistant cuts/slices, that is, 500 different fuel level marks. This simulation resulted in a database with a total of 38,500 rows (with the volume measure and the wetted length of each sensor along every 500 cuts, at each attitude).

Figure 25 shows the behavior of each sensor response considering the 77 different attitudes. The sensors' measurements show a non-linear behavior. Furthermore, each sensor shows a different pattern across the angles, and it is also conditioned to its position. To better visualize and understand Figure 25, other figures are added in Appendix A showing the sensor's behavior under the specific attitude $Pitch = 0°$ and vary all rolls.

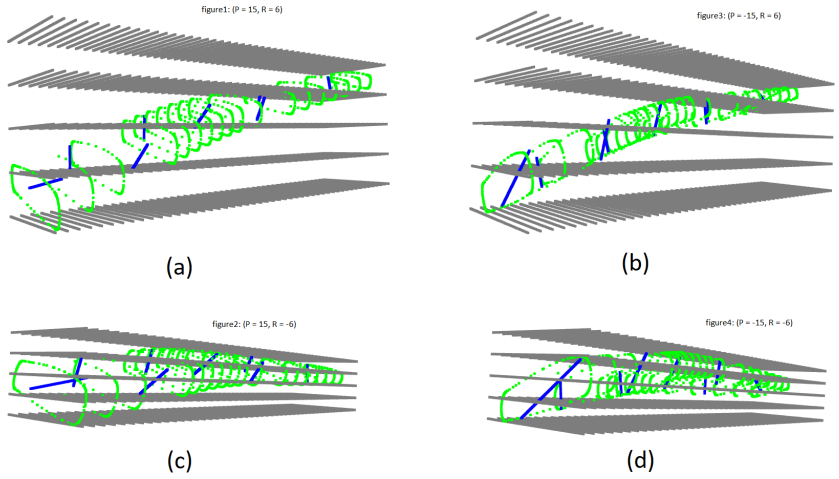

Figure 24. The tool's visualization of the rotated tank and its five slices, developed by the combinations of the following angles: Pitch = $[-15, 15]$ and Roll = $[-6, 6]$. The gray lines depict the fuel surface levels as they intersect with the tank. The tank itself is outlined by the green curves. Within the tank, the blue lines represent the sensors. (**a**) Tank sliced in the attitude (P = 15, R = 6); (**b**) Tank sliced in the attitude (P = −15, R = 6); (**c**) Tank sliced in the attitude (P = 15, R = −6); (**d**) Tank sliced in the attitude (P = −15, R = −6).

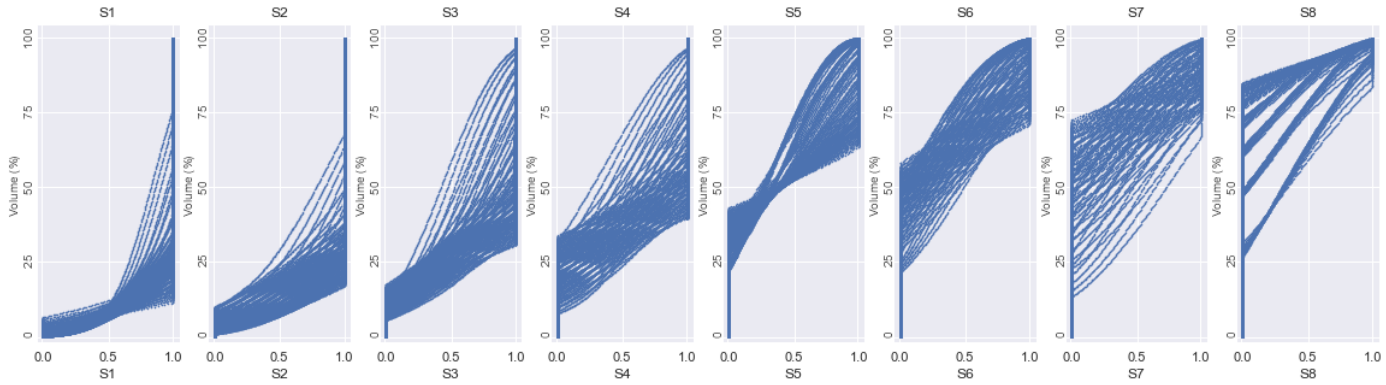

Figure 25. Measurement results from each sensor (S1–S8) inside the fuel tank, in all the 77 different attitudes analyzed. Each subplot contains the behavior of all analyzed attitudes (every curve corresponds to one attitude), with the readings changing from 0 to 1.

It is possible to see how the attitude (Pitch and Roll) influences the behavior of the sensor reading, which consequently influences the mathematical modeling for inferring the measurement of fuel quantity.

5. Conclusions

This study developed an innovative computational tool, combining discretization with descriptive geometry to simulate and gain insights into how aircraft fuel systems and sensor readings behave under various attitudes. This represents a significant advancement in the field, offering a novel approach to understanding fuel levels and sensor responses in aircraft. The tool's ability to generate synthetic sensor data for diverse scenarios and tank geometries is the key aspect to go forward in the development of robust, reliable, and more accurate models for fuel quantity estimation.

The method has been initially tested on regular geometries, such as cubes and spheres. Then, the capability of the tool, under realistic aircraft tank geometry, has been investigated using a generic fuel tank with eight internal-wing strategically placed fuel sensors. The simulation covered combinations of pitches $[-15, 15]^\circ$ and rolls $[-6, 6]^\circ$ and 500 distinct fuel

levels, which resulted in a dataset of over 38,500 records. These data effectively illustrated the sensors' non-linear responses across the various flight conditions, emphasizing the tool's potential in optimizing sensor placement and significantly enhancing the accuracy of fuel quantity modeling in aviation. The nonlinear behavior also highlights the multidimensionality of the phenomena of the aircraft fuel tank quantity measurement problem.

Further evaluation of the performance and accuracy of the computational tool developed in this work will be done using Computational Fluid Dynamics (CFD), which is a powerful tool to analyze the dynamics of fluid flow and cross-validate the relation between sensor readings and continuous change of fluid in the tank subject to changes in attitude.

In conclusion, this study has laid the foundation for future advancements in the field, such as incorporating dynamic models for fuel surfaces, volume estimation models, and optimizing the number and placement of sensors. As part of a wider research project on aircraft fuel quantity estimation, the synthetic data generated by this tool will be instrumental in supporting future work in statistical inference and artificial-intelligence modeling.

Author Contributions: Conceptualization, M.A.D.D.M., V.L.T., C.H.B.M. and J.H.B.; methodology, M.A.D.D.M. and P.G.C.; software, M.A.D.D.M. and P.G.C.; validation, M.A.D.D.M. and P.G.C.; formal analysis, M.A.D.D.M. and P.G.C.; investigation, M.A.D.D.M. and P.G.C.; resources, M.A.D.D.M. and J.H.B.; data curation, M.A.D.D.M. and P.G.C.; writing—original draft preparation, M.A.D.D.M. and P.G.C.; writing—review and editing, M.A.D.D.M., H.N.N., V.L.T., C.H.B.M. and J.H.B.; supervision, H.N.N., V.L.T., C.H.B.M. and J.H.B.; project administration, M.A.D.D.M. and J.H.B.; funding acquisition, M.A.D.D.M. and J.H.B. All authors have read and agreed to the published version of the manuscript.

Funding: The authors acknowledge the funding provided by EMBRAER S.A. and the Brazilian National Council for Scientific and Technological Development (Conselho Nacional de Desenvolvimento Científico e Tecnológico-CNPq). Marcela Di Marzo especially acknowledges the support from CNPq under the CNPq Grant 147629/2019-5.

Data Availability Statement: The data presented in this study are available on request from the corresponding author.

Acknowledgments: The authors also thank the technical support of the EMBRAER engineers: André Katchborian, André Maurice Halal Lombardi, Clayton Rehder, Marcos Fabrício Barros Batistella, and José Armando da Silva.

Conflicts of Interest: Funding for this research was facilitated through a scholarship awarded by EMBRAER S.A. to Marcela Di Marzo, intended for academic and research purposes associated with this manuscript. Viviam Lawrence Takase and Carlos H. B. Mourão were employed by EMBRAER S.A., but their involvement in the study was within their academic and professional capacities, without any additional financial incentives from the company. This arrangement has been made with a clear understanding to uphold the principles of academic integrity and independence in the research process. No aspect of the scholarship or employment by EMBRAER S.A. has influenced the study's design, data analysis, conclusions, or decision to publish. The authors collectively assert that the financial support provided has been strictly for the purpose of facilitating the research, with no conditions that could potentially bias the study's outcomes. The remaining authors have no relevant financial interests to disclose.

Abbreviations

The following abbreviations are used in this manuscript:

AI	Artificial Intelligence
CAD	Computer-Aided Design
FQGS	Fuel Quantity Gauging System
STL	Standard Triangle Language
ST	Surface Triangulation

Appendix A

The supplementary plots (Figures A1–A8) serve to further elucidate Figure 25. They display the variations in sensor readings within the fuel tank under a fixed pitch of 0°, with the roll angle variation between −6° and 6° in 2° increments. Each curve in these plots corresponds to a different roll angle, showing how the sensor's wetted length — presented on the *y*-axis as a normalized value — responds to changes in roll. The *x*-axis quantifies the volume of fuel in cubic meters. The differentiation in the curves accentuates the sensor's responsiveness to varying attitude angles.

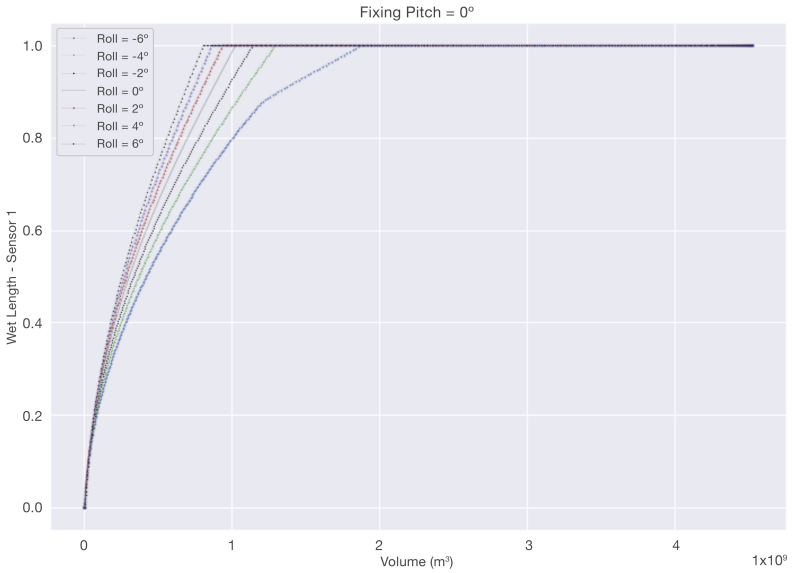

Figure A1. Sensor 1 wetted length response at a fixed pitch of 0° across varying roll angles. The plot displays normalized sensor readings as a function of fuel volume, with each curve corresponding to a different roll angle from −6° to 6°. This visualization highlights the sensor's non-linear response to attitude variations.

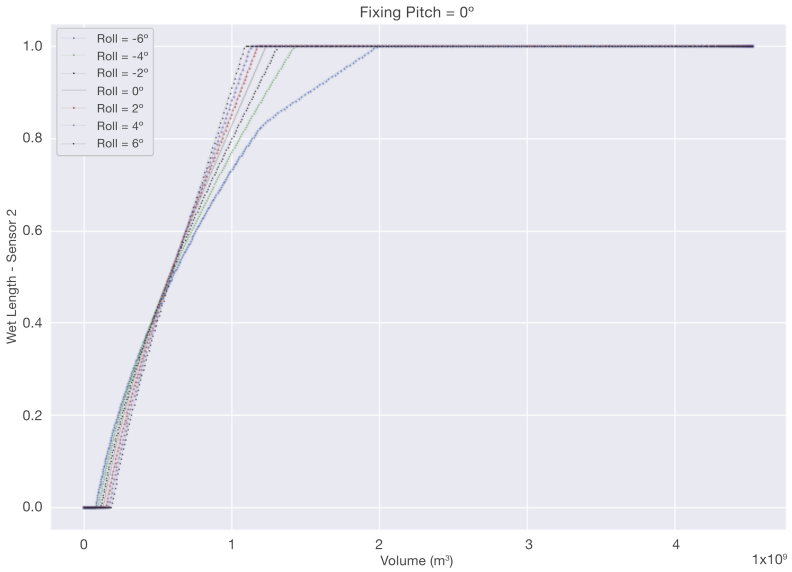

Figure A2. Sensor 2 wetted length response at a fixed pitch of 0° across varying roll angles. The plot displays normalized sensor readings as a function of fuel volume, with each curve corresponding to a different roll angle from −6° to 6°. This visualization highlights the sensor's non-linear response to attitude variations.

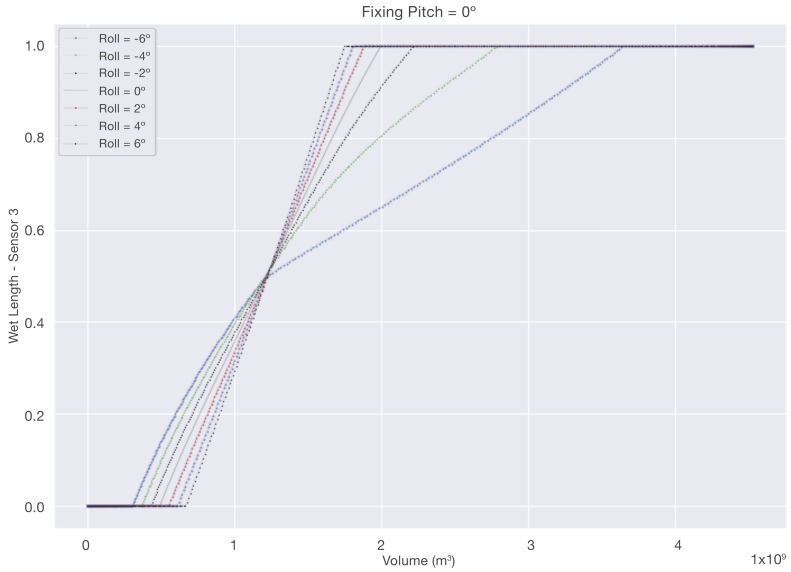

Figure A3. Sensor 3 wetted length response at a fixed pitch of 0° across varying roll angles. The plot displays normalized sensor readings as a function of fuel volume, with each curve corresponding to a different roll angle from −6° to 6°. This visualization highlights the sensor's non-linear response to attitude variations.

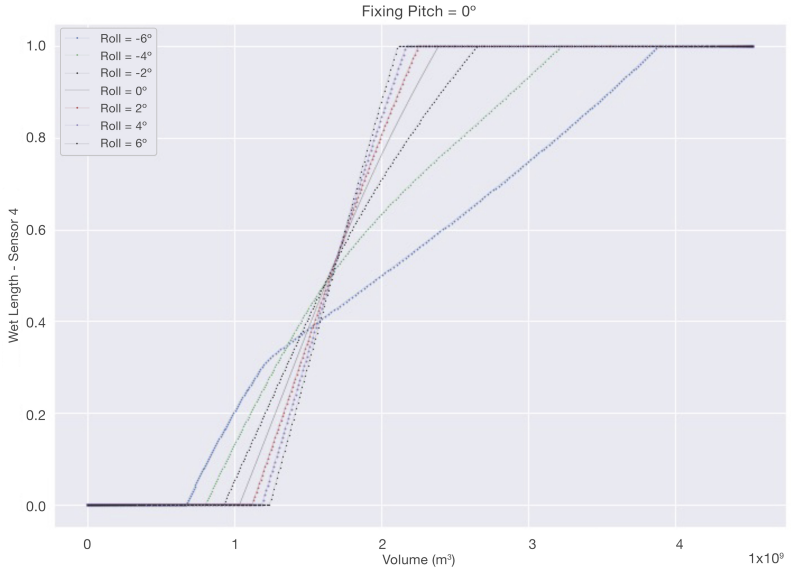

Figure A4. Sensor 4 wetted length response at a fixed pitch of 0° across varying roll angles. The plot displays normalized sensor readings as a function of fuel volume, with each curve corresponding to a different roll angle from −6° to 6°. This visualization highlights the sensor's non-linear response to attitude variations.

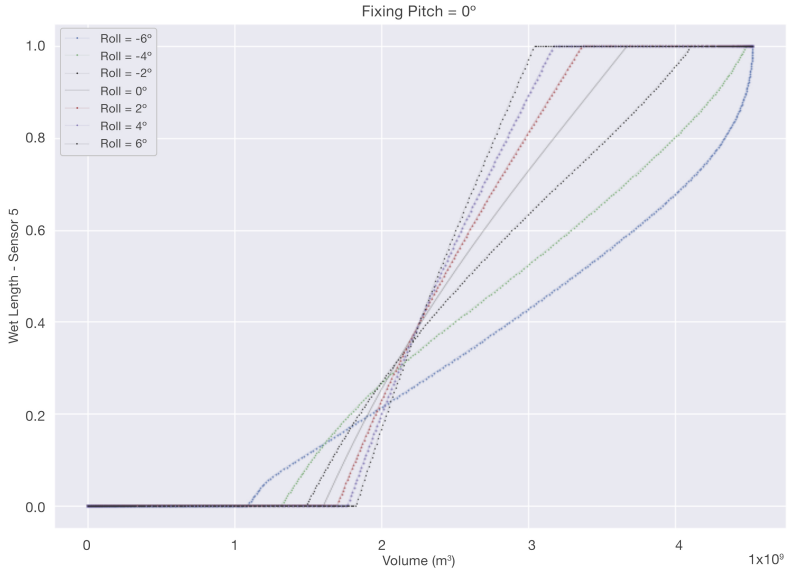

Figure A5. Sensor 5 wetted length response at a fixed pitch of 0° across varying roll angles. The plot displays normalized sensor readings as a function of fuel volume, with each curve corresponding to a different roll angle from −6° to 6°. This visualization highlights the sensor's non-linear response to attitude variations.

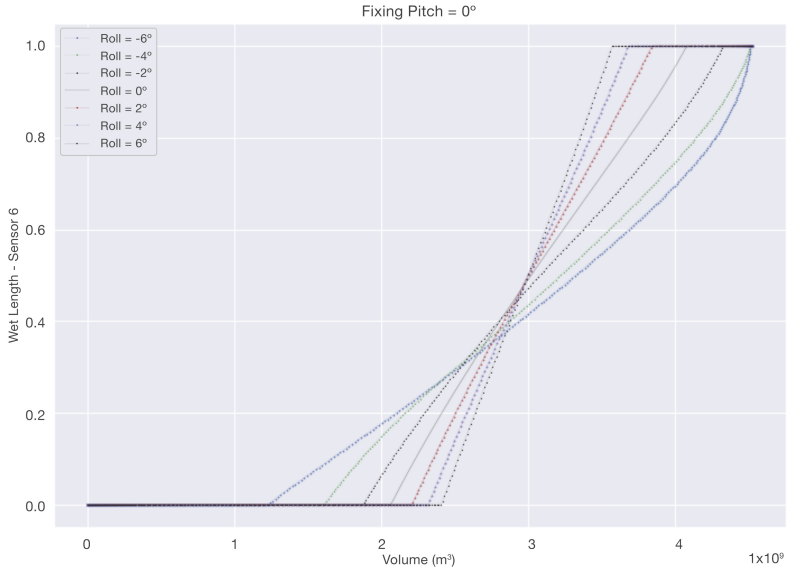

Figure A6. Sensor 6 wetted length response at a fixed pitch of 0° across varying roll angles. The plot displays normalized sensor readings as a function of fuel volume, with each curve corresponding to a different roll angle from −6° to 6°. This visualization highlights the sensor's non-linear response to attitude variations.

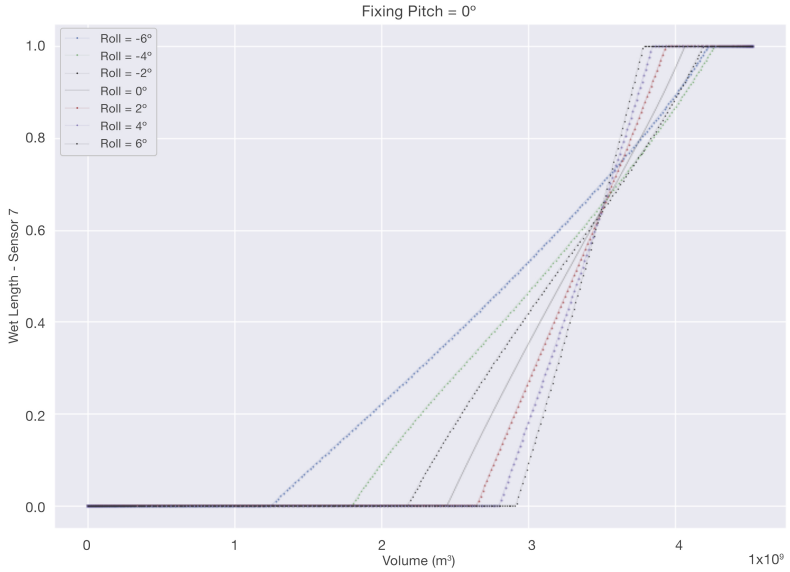

Figure A7. Sensor 7 wetted length response at a fixed pitch of 0° across varying roll angles. The plot displays normalized sensor readings as a function of fuel volume, with each curve corresponding to a different roll angle from −6° to 6°. This visualization highlights the sensor's non-linear response to attitude variations.

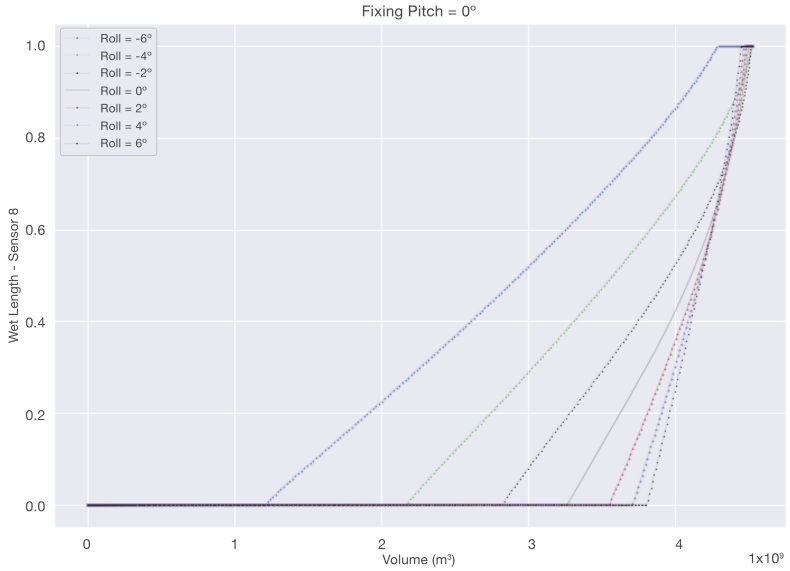

Figure A8. Sensor 8 wetted length response at a fixed pitch of 0° across varying roll angles. The plot displays normalized sensor readings as a function of fuel volume, with each curve corresponding to a different roll angle from −6° to 6°. This visualization highlights the sensor's non-linear response to attitude variations.

References

1. Moir, I.; Seabridge, A. *Aircraft Systems: Mechanical, Electrical, and Avionics Subsystems Integration*; Wiley John & Sons: Hoboken, NJ, USA, 2011; Volume 52.
2. Langton, R.; Clark, C.; Hewitt, M.; Richards, L. Aircraft fuel systems. In *Encyclopedia of Aerospace Engineering*; Wiley John & Sons: Hoboken, NJ, USA, 2010.
3. Zhang, Q.; Lin, G.; Guo, J.; Jin, H.; Zhang, Q. Optimization Research on the Heat Transfer Capacity of an Aircraft Fuel Thermal Management System. *Aerospace* **2023**, *10*, 730. [CrossRef]
4. Ford, T. The Boeing 777 fuel system. *Aircr. Eng. Aerosp. Technol.* **1998**, *70*, 199–202. [CrossRef]
5. Birta, L.G.; Arbez, G. *Modelling and Simulation*; Springer: Berlin/Heidelberg, Germany, 2013.

6. Gill, S.S.; Tuli, S.; Xu, M.; Singh, I.; Singh, K.V.; Lindsay, D.; Tuli, S.; Smirnova, D.; Singh, M.; Jain, U.; et al. Transformative effects of IoT, Blockchain and Artificial Intelligence on cloud computing: Evolution, vision, trends and open challenges. *Internet Things* **2019**, *8*, 100118. [CrossRef]
7. Silling, U. *Aviation of the Future: What Needs to Change to Get Aviation Fit for the Twenty-First Century*; Aviation and Its Management-Global Challenges and Opportunities; IntechOpen: London, UK, 2019.
8. Shmelova, T.; Sterenharz, A.; Dolgikh, S. Artificial Intelligence in Aviation Industries: Methodologies, Education, Applications, and Opportunities. In *Handbook of Research on Artificial Intelligence Applications in the Aviation and Aerospace Industries*; IGI Global: Hershey, PA, USA, 2020; pp. 1–35.
9. Roadmap, A.I. *A Human-Centric Approach to AI in Aviation*; European Aviation Safety Agency: Cologne, Germany, 2020.
10. Jacobs, J.; Goebel, B. The business aviation industry: Growth, contraction and consolidation. *Bus. Econ.* **2020**, *55*, 53–61. [CrossRef]
11. Chakraborty, S.; Chakravorty, T.; Bhatt, V. IoT and AI driven sustainable practices in airlines as enabler of passenger confidence, satisfaction and positive WOM: AI and IoT driven sustainable practice in airline. In Proceedings of the 2021 International Conference on Artificial Intelligence and Smart Systems (ICAIS), Coimbatore, India, 25–27 March 2021; IEEE: Piscataway, NJ, USA, 2021.
12. Rahbari, A.; Rébillat, M.; Mechbal, N.; Canu, S. Unsupervised damage clustering in complex aeronautical composite structures monitored by Lamb waves: An inductive approach. *Eng. Appl. Artif. Intell.* **2021**, *97*, 104099. [CrossRef]
13. García, F.J.; Doblado, J.A.; García, J.M.M.; Álvarez, D.; Vilar, J.R.P.; Sánchez, T.S. Big Data in Aeronautics: Application to the Predictive Maintenance of the Landing Gear. Available online: https://api.semanticscholar.org/CorpusID:219321867 (accessed on 16 April 2024).
14. Zakrzewski, R.R. Fuel volume measurement in aircraft using neural networks. In Proceedings of the IJCNN'01. International Joint Conference on Neural Networks. Proceedings (Cat. No. 01CH37222), Washington, DC, USA, 15–19 July 2001; IEEE: Piscataway, NJ, USA, 2001; Volume 1, pp. 687–692.
15. Zhu, H.; Shao, Y.; Xu, S. Research on aircraft fuel measurement method based on machine vision. In Proceedings of the CSAA/IET International Conference on Aircraft Utility Systems (AUS 2020), Online, 18–21 September 2020; Volume 2020, pp. 1021–1026. [CrossRef]
16. Lee, J.; Kim, B.; Yang, J.; Lee, S. Fuel Quantity Estimation of Aircraft Supplementary Tank Using Markov Chain Monte Carlo Method. *Int. J. Aeronaut. Space Sci.* **2019**, *20*, 1047–1054. [CrossRef]
17. Oliveira, S.P.; Rocha, A.C.; Jorge Filho, T.; Couto, P.R. Uncertainty of measurement by Monte-Carlo simulation and metrological reliability in the evaluation of electric variables of PEMFC and SOFC fuel cells. *Measurement* **2009**, *42*, 1497–1501. [CrossRef]
18. Uzun, M.; Demirezen, M.U.; Inalhan, G. Physics guided deep learning for data-driven aircraft fuel consumption modeling. *Aerospace* **2021**, *8*, 44. [CrossRef]
19. Cui, Z.; Zhong, S.; Yan, Z. Fuel savings model after aero-engine washing based on convolutional neural network prediction. *Measurement* **2020**, *151*, 107180. [CrossRef]
20. Na, G.; Zhi-Hong, Q. Modified particle swarm optimization based algorithm for BP neural network for measuring aircraft remaining fuel volume. In Proceedings of the 31st Chinese Control Conference, Hefei, China, 25–27 July 2012; pp. 3398–3401.
21. Provost, F.; Fawcett, T. Data science and its relationship to big data and data-driven decision making. *Big Data* **2013**, *1*, 51–59. [CrossRef] [PubMed]
22. Wikström, J. 3D Model of Fuel Tank for System Simulation: A Methodology for Combining CAD Models with Simulation Tools. Master's Thesis, Linköping University, Linköping, Sweden, 2011. Available online: https://urn.kb.se/resolve?urn=urn:nbn:se:liu:diva-71370 (accessed on 16 April 2024).
23. Heilemann, F.; Dadashi, A.; Wicke, K. Eeloscope—Towards a Novel Endoscopic System Enabling Digital Aircraft Fuel Tank Maintenance. *Aerospace* **2021**, *8*, 136. [CrossRef]
24. Goraj, Z.; Zakrzewski, P. Aircraft fuel systems and their influence on stability margin. *Pr. Inst. Lotnictwa* **2005**, *4*, 29–40
25. FAA. *Aviation Maintenance Technician Handbook–Powerplant*; FAA: Oklahoma City, OK, USA, 2012; Volumes 1 and 2.
26. Wyatt, D.; Tooley, M. *Aircraft Electrical and Electronic Systems*; Routledge: London, UK, 2018.
27. Langton, R.; Clark, C.; Hewitt, M.; Richards, L.; Moir, I.; Seabridge, A. *Aircraft Fuel Systems*; John Wiley & Sons: Hoboken, NJ, USA, 2009.
28. Gijre, M.M.; Mane, A.; Gadade, R.; Gandhi, S. Smart fuel level indication system. *Glob. Res. Develop. J. Eng* **2017**, *2*, 6.
29. Petlach, P.; Dub, M. Some aspects of COTS ultrasonic fuel level measurement. In Proceedings of the 2017 International Conference on Military Technologies (ICMT), Brno, Czech Republic, 31 May–2 June 2017; IEEE: Piscataway, NJ, USA, 2017.
30. Webster, J.G.; Eren, H. (Eds.) *Measurement, Instrumentation, and Sensors Handbook: Two-Volume Set*; CRC Press: Boca Raton, FL, USA, 2018.
31. Sequeira, A.; Koul, N.; Kumar, A.; Wessely, E.; George, G.; Chakraborty, P. Fuel Level Detector. In Proceedings of the 2019 IEEE International Conference on System, Computation, Automation and and Networking (ICSCAN), Pondicherry, India, 29–30 March 2019; IEEE: Piscataway, NJ, USA, 2019.
32. Kuppusamy, S.; Balachander, K. Embedded based capacitance fuel level sensor. *Elixir Elec. Engg.* **2012**, *43*, 6751–6754.
33. Hanni, J.R.; Venkata, S.K. Does the existing liquid level measurement system cater the requirement of future generation? *Measurement* **2020**, *156*, 107594. [CrossRef]

34. Phillips, W.F.; Hailey, C.E.; Gebert, G.A. Review of attitude representations used for aircraft kinematics. *J. Aircr.* **2001**, *38*, 718–737. [CrossRef]
35. Kane, T.R.; Likins, P.W.; Levinson, D.A. *Spacecraft Dynamics*; McGraw-Hill: New York, NY, USA, 1983.
36. Laila, B.M.; Naveen, N.S. Actuator fault detection in the re-entry phase of an RLV using Kalman filter. In Proceedings of the 2013 International Conference on Control Communication and Computing (ICCC), Thiruvananthapuram, India, 13–15 December 2013; pp. 341–345. [CrossRef]
37. Hughes, P.C. *Spacecraft Attitude Dynamics*; Courier Corporation: North Chelmsford, MA, USA, 2012.
38. Wertz, J.R. *Spacecraft Attitude Determination and Control*; Springer Science & Business Media: Berlin/Heidelberg, Germany, 2012; Volume 73.
39. Nelson, R.C. *Flight Stability and Automatic Control*; WCB/McGraw Hill: New York, NY, USA, 1998; Volume 2.
40. Zienkiewicz, O.C.; Taylor, R.L.; Zhu, J.Z. *The Finite Element Method*; McGraw-hill: London, UK, 1977.
41. Bathe, K.J. *Finite Element Procedures*; Prentice Hall: Upper Saddle River, NJ, USA, 2006; ISBN 9780979004902.
42. Bern, M.; Eppstein, D. Mesh generation and optimal triangulation. In *Computing in Euclidean Geometry 1*; World Scientific: London, UK, 1992; pp. 23–90.
43. Montenegro, R.; Cascón, J.M.; Escobar, J.M.; Rodríguez, E.; Montero, G. Implementation in ALBERTA of an Automatic Tetrahedral Mesh Generator. In *Proceedings of the 15th International Meshing Roundtable*; Springer: Berlin/Heidelberg, Germany, 2006.
44. Mirtich, B. Fast and accurate computation of polyhedral mass properties. *J. Graph. Tools* **1996**, *1*, 31–50. [CrossRef]
45. Eberly, D. Polyhedral Mass Properties (Revisited). 2003. Available online: https://www.magic-sofiware.com/Documentation/PolyhedratMassProperties.pdf (accessed on 16 April 2024).
46. Salviano, D.F. Modelling and Simulation of Aircraft Fuel Tank Gauging. Master's Thesis, Instituto Tecnológico de Aeronáutica (ITA), São José dos Campos, SP, Brazil, 2018.
47. Clinciu, R. Teaching basics of the descriptive geometry-relative positions of lines and planes. *J. Ind. Des. Eng. Graph.* **2015**, *10*, 9–12.
48. McCrea, W.H. *Analytical Geometry of Three Dimensions*; Courier Corporation: North Chelmsford, MA, USA, 2012.
49. Boulos, P.; de Camargo, I. Geometria analítica. *CEP* **1987**, *4533*, 1–387.
50. Cramer, G. *Introduction à l'Analyse des Lignes Courbes Algébriques*; Chez les frères Cramer et C. Philibert: Geneva, Switzerland, 1750.
51. Warner, S. *Modern Algebra*; Courier Corporation: North Chelmsford, MA, USA, 1990.
52. Schetz, J.A.; Fuhs, A.E. (Eds.) *Fundamentals of Fluid Mechanics*; John Wiley & Sons: Hoboken, NJ, USA, 1999.
53. Swokowski, E.W. *Calculus with Analytic Geometry*; Taylor & Francis: Abingdon, UK, 1979.
54. Harris, J.W.; Stöcker, H. *Handbook of Mathematics and Computational Science*; Springer Science & Business Media: Berlin/Heidelberg, Germany, 1998.